# Ceria nanorod supported gold nanoparticles as structured catalysts for the oxidative steam reforming of methanol: Effect of CTAB concentration on physiochemical properties and catalyst performance

Srisin Eaimsumang[a], Nuwong Chollacoop[b], Apanee Luengnaruemitchai [a,c*],

Stuart H. Taylor[d]

[a] *The Petroleum and Petrochemical College, Chulalongkorn University, Pathumwan, Bangkok 10330, Thailand*

[b] *Renewable Energy Laboratory, National Metal and Materials Technology Center (MTEC), 114 Thailand Science Park, Klong Luang, Pathumthani 12120, Thailand*

[c] *Center of Excellence in Catalysis for Bioenergy and Renewable Chemicals (CBRC), Chulalongkorn University, Bangkok 10330, Thailand*

[d] *Cardiff Catalysis Institute, School of Chemistry, Cardiff University, Main Building, Park Place, Cardiff, CF10 3AT, UK*

* Corresponding author. Tel.: +662-218-4147; Fax: +662-611-7220; E-mail: apanee.l@chula.ac.th

**Abstract**

Ceria ($CeO_2$) supports were synthesized by hydrothermal treatment with different Cetyltrimethyl ammonium bromide (CTAB) concentrations ($CeO_2$-X: 0.135, 0.270, 0.540 and 1.080, where X is the CTAB concentration in mmol). The micro-structures of bundle-like ceria nanorods (NR) were produced by thermal treatment of the crystalline $Ce(OH)CO_3$ precursor. The exposed crystal planes of (200) and (111), corresponding to the d-spacing of 0.27 and 0.31 nm, were confirmed by high resolution-transmission electron microscopy (HR-TEM). The fundamental characteristics of $CeO_2$-0.135 led to the highest surface area, surface area normalized reducibility and oxidized gold species ($Au^{n+}/Au^0$) on the surface, relatively higher oxygen vacancies and a smaller average gold particle size (7.9 nm). The activity results show that the Au/$CeO_2$-0.135 has the highest methanol conversion and $H_2$ production rate for oxidative steam reforming of methanol (OSRM). The reducibility and gold particle size played a crucial role in determining the $H_2/CO_2$ ratio at the temperature of 200°C.

*Keywords:* Methanol; Hydrogen; OSRM; CTAB; gold; ceria nanorod

## 1. Introduction

Gold nanoparticles supported on $CeO_2$ have been regarded as an effective catalyst for steam reforming of methanol (SRM)[1], water-gas shift (WGS)[2-4] and many oxidation reactions [5-8] in terms of providing high conversion at lower reaction temperature compared to other catalysts. One of the applications for this catalyst is steam reforming of methanol for $H_2$ production, due to the synergistic function of gold on an active support like $CeO_2$. SRM can provide a high $H_2$ yield, and it can also produce higher CO formation compared to partial oxidation of methanol (POM).

Moreover, it requires a significant supply of energy, due to it being an endothermic reaction. Therefore, oxidative steam reforming of methanol (OSRM) has been introduced as a selective reaction, but it does have the compromise of being able to produce high yields of $H_2$, while producing a lower yield of CO when the oxidation reaction predominated. Pojanavaraphan *et al.* investigated the effect of $O_2$ content on the activity of $Au/CeO_2$ catalysts in OSRM reaction at 200-400ºC [9]. The $CO_2$ selectivity increase as a result of significant taking place of POM reaction. Furthermore, OSRM has the advantage of being able to supply energy, as it is an exothermic oxidation reaction. However, the product distribution (e.g. $H_2$, CO and $CO_2$) depends on the feed composition, as shown in Eq (1):

$$CH_3OH + (1\text{-}a)H_2O + 0.5aO_2 \rightarrow CO_2 + (3\text{-}a)H_2 \quad (1)$$

$$\Delta H^{\circ}_{298} = \text{-}192.2\text{-}49.5 \text{ kJ/mol}; (0 < a < 1)$$

Au supported on ceria nanorods (NR) has provided the best catalytic activity for many reactions, such as preferential oxidation of CO (CO-PROX)[7], WGS [2], SRM [1], and OSRM [10]. This is because of the high surface area to volume ratio and exposure of the active (110) and (100) planes, leading to the highest reducibility and oxygen vacancies. In addition, ceria NR influence the characteristics of gold nanoparticles, for example, gold particle size, oxidation state and dispersion, including interaction between metal and support. These properties promote superior catalytic activity when compared to other ceria nanoshapes. Ceria has beenclassified as an active support because of its oxygen mobility, as oxygen can be exchanged from the structure depending on temperature, resulting in the inverted conversion between $Ce^{4+}$ and $Ce^{3+}$, consequently generating oxygen vacancies. This property strongly relates to various factors, namely, crystallite size, morphology and exposed crystal plane. Typically, for an fcc structure, ceria surfaces consist of three main low-index crystal planes: (111), (110) and (100), which have

different surface energies. The active surfaces have the order: (100) > (110) > (111), regarded as the surface free energy of 2.05, 1.26 and 0.69 eV, respectively [11]. However, the energy for formation of oxygen vacancies can be ordered as (110) < (100) < (111) with respect to 1.99, 2.27 and 2.6 eV, respectively [12].

Typically, single crystalline ceria nanorods (NR) are obtained randomly, formed by particle agglomeration, which is the case without assisted synthesis using a template. However, bundle-like structures of ceria NR can be designed by thermal conversion of a single crystal of $Ce(OH)CO_3$ [13]. This structure can yield many advantages, because it is composed of a multilayer structure and active surface, (100), and has a high aspect ratio, and high surface area to volume ratio. To control size and morphological structure of ceria NR, a hydrothermal synthesis method is a simple way to obtain the desired morphology of the nanomaterial. Nevertheless, particle agglomeration and large size distribution can result under the high temperature and pressure used for hydrothermal synthesis, leading to a lower surface area. To solve this problem, the addition of organic molecules during synthesis can prevent particle agglomeration, by means of stabilizing adsorption on particular surfaces, and through beneficial steric hindrance it can direct crystal growth. Cetyltrimethylammonium bromide (CTAB) is one of the surfactants that is commonly used for catalyst synthesis. However, the concentration during catalyst synthesis should be optimized to obtain the best ceria properties for catalysis. Previously, the effect of CTAB to ceria precursor ratio on the textural properties of ceria has been studied, but the role of using surfactant during synthesis was still not fully explored [14].

To clarify the effects of morphology on the catalytic performance of ceria NR, we synthesized ceria NR using CTAB as a template, and studied the role of varying CTAB surfactant concentrations on ceria morphology and physiochemical characteristics. The range of ceria NR

synthesized was used as a support to prepare 3 wt% Au/$CeO_2$ catalysts. All catalysts were characterized by various techniques and the catalytic performance was evaluated for OSRM performance.

## 2. Experimental

### *2.1. Catalyst preparation*

The desired amount of CTAB (Aldrich, 96%), 2.3 mmol of $Ce(NO_3)_3 \cdot 6H_2O$ and 9.2 mmol of urea were dissolved in 10 mL of deionized water at room temperature under agitation for 15 min. The solution was then put into a 125-mL Teflon-lined stainless-steel autoclave and maintained at 120˚C for 12 h. After cooling, the white slurry was collected by filtration, washed thoroughly with excess deionized water to eliminate residual ions and dried in an oven at 80°C for 24 h. Finally, the white powder was calcined in static air at 500°C for 10 h. The $CeO_2$ support was denoted as $CeO_2$-X, where X is the CTAB concentration in mmol.

The Au/$CeO_2$-X (3 wt%Au) catalysts were prepared by the deposition-precipitation method. Accordingly, the $CeO_2$-X powder was added in an aqueous solution of 2 mmol/L hydrogen tetrachloroauric (III) acid ($HAuCl_4 \cdot 3H_2O$; 99.99%, Alfa-Aesar) under continuous stirring at room temperature for 1 h. Meanwhile, 0.1 mol/L of $(NH_4)_2CO_3$ was added dropwise to control pH of the solution~8.5 [10]. The precipitate was then washed by deionized water until pH 7 was attained and then collected by filtration. It was finally dried under vacuum at 80°C for 16 h and calcined in static air at 400°C for 4 h.

*2.2. Catalyst characterization*

The surface area of catalysts was determined by $N_2$-physisorption at -196 °C, using a Quantachrome Autosorb-1 surface area analyzer. The specific surface area of catalysts was determined by the Brunauer-Emmett-Teller (BET) equation. Prior to the measurements, all samples were degassed under vacuum circumstance at 250°C for 16 h.

X-ray diffraction (XRD) was used to identify the crystalline structure of $CeO_2$-X supports and Au/$CeO_2$-X using a Rigaku X-ray diffractometer system (RINT-2200) equipped with Cu Kα radiation, operated at an accelerating voltage of 40 kV and 30 mA current. The analysis was continuously scanned with a speed of 2θ equal to 5°/min and a scan step of 0.02˚ (2θ), 2θ range was from 20 to 80°. Crystallite size (D) calculations of the Au(111) and $CeO_2$(111) were done using the Scherrer equation: $D=(0.94\times\lambda)/(\beta\times\cos\theta)$, where λ is the wavelength of the Cu Kα (0.15406 nm), β is the full width at half the maximum (FWHM) of the X-ray diffraction peak, and θ is the Bragg angle at corresponding peak (deg).

The morphological structure of the $CeO_2$-X supports was investigated by field emission gun scanning electron microscopy (FEG-SEM) using a Tescan MAIA3 microscope. The samples were coated by Au:Pt at a ratio of 80:20 (%v) with a thickness of 10 nm.

High resolution transmission electron microscopy (HR-TEM) was utilized for identifying the morphologies and exposed crystal planes of the catalysts. The analysis was performed by using a JEOL JEM-2100 instrument operated at a 200 kV.

$H_2$-temperature-programmed reduction (TPR) analysis was used to measure the reducibility of the catalysts. Approximately 0.1 g of sample was contained in a quartz tube reactor and analyzed using a TPDRO 1100 instrument (Thermo Finnigan) equipped with a thermal conductivity detector

(TCD) The measurement was performed with 5.13% $H_2$ in Ar at 30 mL/min. The reduction temperature was raised from 30 to 900°C with a heating rate of 10°C/min.

X-ray photoelectron spectroscopy (XPS) was utilized to analyze the elemental composition on the surface and oxidation state of material using a Kratos Axis Ultra DLD photoelectron spectrometer equipped with a monochromatic Al Kα radiation operated at 15 kV under a pressure of less than $5\times10^{-7}$ Torr. All XPS spectra were calibrated by the C 1s (284.6 eV). The obtained XP spectra was analyzed by the vision processing software supplied with the instrument. The Shirley background was applied to normalize peaks of the XP spectra. The peak position of Au varied about ±0.3 eV and maintained the FWHM. The spin orbit splitting of Au4f was at about 3.7eV. The peak of O1s and Ce3d were fitted by a Lorentzian Asymmetric Lineshape with a varied FWHM due to the asymmetric peak.

Raman spectroscopy was used to observe the vibrational properties of catalysts using a Renishaw InVia Raman spectrometer, at a power of 10 mW and a laser excitation source of wavelength 514 nm with a spectral resolution of 1 $cm^{-1}$.

The quantification of actual gold loading for each catalyst was measured by an inductively coupled plasma-optical emission spectroscopy (ICP-OES) technique on a Perkin Elmer Optima 4300 D, using $Ar/N_2$ plasma. Approximately 7.5 mg of $Au/CeO_2$-X samples were digested by aqua regia solution (HCl 37% (Aldrich)/$HNO_3$ 67% (Aldrich) : 3/1) at 70 °C under agitation for 20 min. The solution was filtered to eliminate residual particles and the final volume was subsequently adjusted to 100 mL with deionized water.

*2.3. Catalytic activity measurement*

Approximately 100 mg of catalyst was packed into the 6 mm inner diameter quartz reactor tube, which was performed under atmospheric pressure over a reaction temperature of 100 and the range 200 - 400°C, with a constant 0.6/2/1 molar ratio of oxygen/water/methanol (MeOH). A constant flow rate of distilled water and MeOH mixture was controlled by a syringe pump at 1.5 mL/h, and vaporized by passing through a pre-heater, accompanied by He (45 mL/min) as a carrier gas, and then mixed with the $O_2$ (5 mL/min) stream before entering the reaction zone. A gas hourly space velocity (GHSV) was preserved at 30000 mL/$g_{cat}$·h. The gaseous product composition (e.g. $H_2$, $CO_2$, $CH_4$ and CO) was analyzed by gas chromatography (GC) using an Agilent 6890N GC system equipped with a TCD and a carbosphere column. The condensates (e.g. MeOH) were identified by GC using an Agilent 7890A GC system equipped with a flame ionization detector and a DB-wax column[10]. The methanol conversion (*X*) and product selectivities were obtained from Eqs. 2-3:

$$X = \frac{C_{MeOH}^{in} - C_{MeOH}^{out}}{C_{MeOH}^{in}} \times 100(\%) \quad (2)$$

$$S_i = n_i / \sum n_i \times 100\ (\%) \quad (3)$$

where, i represented the gas product, namely, $H_2$, CO, $CO_2$ and $CH_4$ and n denoted as the rate of gas produced in mole.

## 3. Results and discussion

### *3.1 Characterization*

#### *3.1.1. XRD analysis*

All the calcined ceria catalyst structures were ascribed to the fluorite cubic $CeO_2$ structure (ICDD card number 01-078-5328), due to corresponding diffraction peaks of (111), (200), (220),

(311), (222), (400), (331) and (420) planes, respectively, as presented in Fig. 1. The crystallite size of the parent ceria, as determined by X-ray line broadening, did not alter with the variation of the CTAB concentration, as it was in the range of 11.8-12.4 nm. Therefore, CTAB concentration did not significantly affect the crystal growth phenomena of ceria. The crystal size of ceria in the presence of Au was slightly increased, probably due to the second heat treatment from calcination. All ceria crystallite sizes were in the range of 12.0-13.4 nm. In addition, the corresponding diffraction peak of Au(111), indicative of $Au^0$, can be detected at 2-Theta of about 38.2°for all catalysts [15]. Subsequently, gold crystallite sizes were also calculated using the Sherrer equation. They were in the range of 8.3-11.9 nm.

*3.1.2. Textural properties*

$N_2$ adsorption-desorption isotherms for the synthesized ceria (Fig. SI1) represent those typical of porous materials. They exhibited type II Isotherms according to the IUPAC system, where monolayer adsorption predominantly takes place at a low relative pressure, while multilayer adsorption occurs at higher relative pressure. In addition, the capillary condensation occurred at $P/P_0 = 0.4$, which belonged to type H4, representing agglomeration of particles forming slit shaped pores [16]. The textural properties of all catalysts were determined. Ceria prepared without CTAB had a lower BET surface area (56 $m^2/g$), as shown in Table 1, than those with CTAB added during synthesis, and this is in agreement with previous studies [14]. It is clear that addition of CTAB reduced particle agglomeration, as CTAB is adsorbed on the cerium oxide surface by electrostatic interaction between alkylammonium ion and nucleophilic oxide of the ceria [17]. The BET surface area of parent ceria increased with increasing CTAB concentration and approached the highest value at 90 $m^2/g$ for $CeO_2$-0.270, and then subsequently decreased 1.2-fold for $CeO_2$-0.540. The

high excess of the CTAB molecule adsorbing on the ceria surface might result in the decrease of dissolution and recrystallization rate. The surface area of the final catalysts was slightly reduced, by about 8-15%, after gold deposition.

*3.1.3. Ceria morphology (SEM and HR-TEM analysis)*

The morphological structure of the ceria was examined by SEM. The results showed that they exhibited a flower-like morphology, which was composed from a bunch of nanorods. This morphology was also synthesized by a $Ce(OH)CO_3$ route in the presence of CTAB at 100°C for 24 h, as previously reported [13]. To investigate the effect of CTAB on inducing ceria morphology, SEM images of ceria prepared without CTAB are presented in Fig. 2e. The morphology shows some similarity, with many groups of nanorods adhering together, but forming more dense-particle agglomerates with a more non-uniform direction of rods. Comparing ceria morphologies prepared in the presence of CTAB, the dimension of the micro-flower structures was relatively larger for higher concentrations of CTAB when compared to lower CTAB concentrations. The capability of CTAB to act as a stabilizer restricts the growth of ceria particles, because it reduces the surface tension of ceria particles, leading to a reduction of dissolution/recrystallization during hydrothermal synthesis. It was evident that CTAB did not have a significant role in altering ceria morphology, but it did improve some physical properties. When surfactant concentration was less than $10^{-5}$ M, electrostatic interaction between metal ions and organic ions is rather weak. Hence, this is the reason it does not directly manipulate morphologies [18].

The crystallographic planes of $Au/CeO_2$ catalysts were indexed from the HR-TEM images (Fig. 3). Principally, the rod-like ceria mainly consisted of the (111) and (200) indexed planes, identified from the measured d-spacings of 0.31 nm and 0.27 nm, respectively. The tip of the rods

exposed the most stable crystal plane of (111), visible from Fig. 3g, while the crystal planes of (200) were mostly perpendicular to the (111) planes on the stem of the rods. Furthermore, the existence of crystalline gold nanoparticles was found for Au/$CeO_2$-0.135, where the crystal planes of Au (111) and Au (200), corresponding to the d-spacings of 0.235 and 0.200 nm, respectively, appeared on the higher surface energy (200) crystal plane of ceria, as shown in Fig. 3a. Likewise, the crystal plane of Au (111) and Au (200) were noted for Au/$CeO_2$-0.270. Only Au (111) was observed, located on the ceria (111) crystal plane, in the case of Au/$CeO_2$-0.540 and Au/$CeO_2$-1.080. For the FCC structure, the low-index $CeO_2$ crystal plane consisted of (111), (100) and (110), which (110) and (100) had higher surface energy than (111). The different surface energy of those planes resulted from the different exposed atomic arrangement. $CeO_2$(111) surface had repeating unit of atom on 3 planes in a symmetric axis position leading to no net dipole moment perpendicular on the surface. Whereas, (110) and (100) had atomic configuration only 2 planes generating dipole moment perpendicular on those surfaces [11]. It was postulated that different CTAB concentrations during synthesis influenced the location of gold deposition and the exposed Au crystalline phases on the specific ceria crystal plane. In addition to investigating the crystallographic planes of the catalyst, the actual gold particles sizes were estimated from particles size distribution data obtained from HR-TEM images. It seems that a larger gold particle size was present on ceria catalysts synthesized with higher CTAB concentrations, following the order: Au/$CeO_2$-0.270 < Au/$CeO_2$-0.135 < Au/$CeO_2$-0.540 < Au/$CeO_2$-1.080. The summary of mean gold particle size is shown in Table 1, gold particle sizes ranged from 7.8-13.1 nm.

Typically, the crystallization under hydrothermal treatment consisted of a nucleation and crystal growth step, *via* an Ostwald ripening process [19]. When CTAB concentration is lower than the CMC value, it does not form a micelle in the aqueous solution. Hence, below the CMC a

single CTAB molecule might adsorb on a non-specific surface of ceria and prevent agglomeration by steric hindrance of the tail group. The growth habit would still follow the Ostwald ripening process, in which small crystals are thermodynamically unstable and dissolve in the solution and then recrystallize on the larger particles. Nevertheless, the higher concentration of surfactant adsorbed on the surface retarded the Ostwald ripening process, due to the fact that the particles were more stable and difficult to dissolve [20]. Therefore, when the particles cannot dissolve and then recrystallize, the particles tend to gather together as a bulky group in order to be more stable thermodynamically. As a result, larger particle sizes and lower surface areas were observed.

The crystallite size mainly relates to the nucleation rate, which involved the diffusion of ions to the growing crystal surface and incorporation of the nucleus into the structure of the crystal lattice [21]. The nucleation process of $Ce(OH)CO_3$ was started by reaction between hydrolyzed $Ce^{3+}$ ion with water to form the complex $[Ce(OH)(H_2O)_{n-1}]^{2+}$ and carbonate ion ($CO_3^{2-}$), decomposed from urea at the temperature used [22]. Fundamentally, in the aqueous solution the diffusion rate of ions is really fast due to very low solution viscosity [21]. When the amount of CTAB increased in the solution, it might suppress the hydrolyzation of $Ce^{3+}$ ion with a water molecule to form $[Ce(OH)(H_2O)_{n-1}]^{2+}$, and reduce formation in the aqueous medium. Therefore, the higher volume of surfactant might reduce the diffusion rate of ions, resulting in a slower nucleation rate and extent of nucleation, consequently leading to a larger particle size.

*3.1.4. Reducibility of catalysts*

The reducibility of ceria was determined by $H_2$-TPR. The reduction of active oxygen from the ceria structure at the surface and the bulk, represented by the reduction features at temperatures of about 520°C and 850 °C, respectively, as illustrated in Fig. SI2. The reduction temperatures of all

the ceria samples were similar, however, slightly different $H_2$-uptakes (0.42-0.50 mmol/g) were evident (Table 2). These results correlated with the similar physical properties, such as crystallite size and BET surface area. Interestingly, the surface reduction temperature was decreased to much lower values(145-154°C) after gold deposition, which resulted from weakening of the Ce-O bond in the presence of gold [23]. The magnitude of $H_2$ uptake represents improved redox properties for activating molecular oxygen and the interaction between metal and support. The $H_2$ consumption significantly increased by 1.2-1.7-fold for all Au/$CeO_2$-X catalysts when compared to the parent ceria, except for Au/$CeO_2$-0.540. Au/$CeO_2$-0.135 exhibited the highest $H_2$ uptake (0.82 mmol $H_2$/g), which was 1.7 times greater than for pure ceria.

*3.1.5. Raman analysis*

The symmetrical vibration of lattice oxygen of the prepared catalysts was investigated by Raman. The Raman spectra of both ceria and Au/$CeO_2$-X catalysts are given in Fig 4. The small peak at 259 $cm^{-1}$ was reported as a second-order transverse acoustic mode of $CeO_2$ [24]. A strong $F_{2g}$ band at about 464 $cm^{-1}$ was assigned to the symmetric stretching vibration of linked Ce-O bonds, whilst the band around 600 $cm^{-1}$ was due to defect sites or intrinsic oxygen vacancies in the ceria structure [25]. The weak band positioned at about 1170 $cm^{-1}$ corresponded to the second-order longitudinal optical mode of defects [26]. For ceria catalysts containing gold, the $F_{2g}$ band located at 464 $cm^{-1}$ became broader, measured by an increase of the FWHM for all gold catalysts, compared to that of the parent ceria. Moreover, the bands at around 600 $cm^{-1}$ were hardly visible (Fig. 4b), they became broader and lower in intensity, probably because the addition of Au caused a more asymmetric vibrational band, due to the weakening of the Ce-O bond. Moreover, the weak bands at 259 $cm^{-1}$ gradually shifted toward lower wavenumbers in the case of Au/$CeO_2$-X prepared

with lower concentrations of CTAB. The vibrational bands at about 830-837 $cm^{-1}$ appeared in the gold-containing catalyst series, corresponding to the presence of peroxide species ($O_2^{2-}$) generated on $CeO_{2-x}$ (111) [27]. Au deposition influenced the properties of the ceria. Comparing the concentration of ceria intrinsic oxygen vacancy sites, by means of comparing the peak area ratios ($A_{600}+A_{1170}/A_{464}$), between the defect band and $F_{2g}$ band. The results are presented in Fig. 5b. There were no significant differences for $CeO_2$-X catalysts that did not contain gold. However, the concentration of oxygen vacancy sites was considerably enhanced in the case of Au/$CeO_2$-0.135 and Au/$CeO_2$-0.270. Gold deposited onto ceria synthesized with higher CTAB concentrations only had slightly increased numbers of oxygen vacancy sites, about a 6.4-9.6% increase. An increase defect concentration resulted from the perturbation of the ceria lattice oxygen by gold deposition and consequently developed oxygen vacancies in the ceria supports [28, 29].

*3.1.6. ICP and XPS analysis*

The actual gold loading was measured by ICP-EOS. The results show that the actual gold loading was slightly less than the nominal gold loading (3 wt.%,), and measured gold content was in the range 2.29-2.45 wt.%. Au/$CeO_2$-0.270 had the highest gold content of 2.45 wt.%. Additionally, the surface gold concentration was also investigated by XPS. Gold was found on the surface at 0.8-1.3 at.%. Au/$CeO_2$-0.135 had the highest amount of gold on the surface. It can be briefly described that the high surface area of the $CeO_2$-0.135 contributed to an increased nucleation site for gold deposition.

The electronic states of elements on the catalyst surface were also examined by XPS. The oxidation state of cerium, present as $Ce^{3+}$ and $Ce^{4+}$, was differentiated by peak fitting of the Ce 3d spectra as demonstrated in Fig. SI3. The predominant peaks located at lower binding energies of

882.0, 889.0 and 898.3, were classified as characteristic of Ce $3d_{5/2}$. The higher binding energies of 900.5, 907.7 and 916.5 eV are characteristic of the Ce $3d_{3/2}$ spin-orbit components. The two spin-orbit coupled doublets of $Ce^{3+}$ were indexed with a BE of 880.5,885.7, 899.7 and 902.3 (denoted as v symbol), respectively. Furthermore, the surface percentage $Ce^{3+}$ content was calculated. The results demonstrated that $Ce^{3+}$ contents was consistent for the series of parent ceria supports, and were in the range 11.4-14.8%. Interestingly, it was noticeably different in the case of the gold catalysts. Au/$CeO_2$-0.135 and Au/$CeO_2$-1.080 had the greatest surface $Ce^{3+}$ contents, with 23.5 and 22.1 % respectively.

The surface oxidation state of Au was also measured by the XPS technique in order to studied the characteristics of gold on the different ceria supports. The XP spectra of Au $4f_{5/2}$ and Au $4f_{7/2}$ are shown in Fig. 6, and these consist of a main pair of peaks located at BEs of 83.8 and 87.5 eV, representing metallic Au ($Au^0$). Whereas, the latter two peaks at BEs of 84.9 and 88.7 eV, were assigned to $Au^+$. $Au^{3+}$ was expected at a higher BE of 86.3 and 89.9 eV [15]. Moreover, the ratio of $Au^{n+}/Au^0$ was also calculated by means of the ratio of appropriate peak areas, as concluded in Table 3. There was a tendency for surface $Au^{n+}/Au^0$ to decrease as the concentration of CTAB in the ceria synthesis procedure increased. Au/$CeO_2$-0.135 had the highest $Au^{n+}/Au^0$ ratio of 0.43. The presence of gold oxide indicated the cationic gold locating at the interface between Au and support with chemical bonding Au-O-Ce, where the metallic Au was above this layer as a model, was reported in [30] , and in this study we consider the same is present in the catalysts.

Surface oxygen species were also differentiated by analysis of the XP spectra of the O1s signal (Fig. 7). Peak fitting identified 3 surface oxygen species classified as, lattice surface oxygen of ceria (529.0 eV), whereas peaks existing at 531.0 and 533.0 eV were ascribed to a defect site, and an adsorbed oxygen species and/or a hydroxyl group, respectively [31]. The results found that the

ratio of surface lattice oxygen tentatively declined for Au/$CeO_2$-X catalysts, when X>0.135. This result might correspond to the effect of gold particle size and the nature of the support. The smaller gold particle size on the ceria support has a higher surface area, and thereby the lattice oxygen is more available on the ceria surface. Moreover, a higher amount of surfactant in the solution led to slower diffusion of ions to the crystal surface, reducing nucleus formation of oxide, corresponding to a lower intensity of the lattice oxygen peak (Fig. 7), when compared to the ones synthesized with a lower amount of CTAB.

*3.2. Catalyst performance*

The parent ceria and Au/$CeO_2$ catalysts series were examined for their catalytic activity for the OSRM reaction between 200-400°C. The methanol conversion and $H_2$ production rates were evaluated and are shown in Fig. 8. The reactivity of ceria only catalysts did not demonstrate any significant difference in both methanol conversion and $H_2$ production rate. The methanol conversion was very low at 250°C, and was due to combustion, with only $CO_2$ and CO produced. Oxygen in the feed stream was completely consumed at 300°C, and therefore above this temperature methanol conversion resulted in the formation of $H_2$. The methanol conversion continuously increased with increasing reaction temperature, reaching the highest value (86-93%) at 400°C. All methanol conversion exceeded the maximum conversion of 68%, which is the theoretical maximum if partial oxidation of methanol (POM) is the only reaction operating, indicating that there was also the reaction of methanol steam reforming or methanol decomposition competing. The catalytic performance of Au/$CeO_2$-X catalysts lowered the temperature for activity significantly when compared to the activity of the parent ceria supports, as activity was observed at temperatures around 200°C lower when Au was added. The gold-containing catalysts provided high methanol conversion, in the range 80-90%, from 200°C. The methanol conversion increased

with increasing reaction temperature up to 400°C, and almost 100% methanol conversion was achieved for the gold catalyst series. The performance of $Au/CeO_2$-X catalyst is compared to that of non-noble metal catalysts for OSRM reaction. The 6 wt% $Cu/CeO_2$ can achieved 100% MeOH conversion at 230°C but $H_2$ selectivity was the highest at about 26% [32]. The 70 at% $CuO/CeO_2$ provided 100% conversion from 200°C but CO selectivity was higher than 6% at 300ºC [33]. The bimetallic 3% $Ni/Cu/ZrO_2$ performed only at about 60% MeOH conversion at 400ºC and CO selectivity was dominant and was as high as 90% [34]. The methanol conversion was complete only at 400ºC for 8.3% $CuO/CeO_2/Al_2O_3$ [35]. 20% $CuO/CeO_2/Al_2O_3$ also achieved 100% conversion in oxy-reforming of methanol at 200 ºC, as reported by Mierczynski *et al.*[36]. Based on these literature data, Cu catalysts were very active for OSRM reaction that can reach the complete MeOH conversion at lower temperature than the present work. However, the copper loading was much higher than required for Au catalysts in order to obtain the maximum conversion.

The rate of $H_2$ production was also studied, the parent ceria initially generated $H_2$ at 300°C, correlating to the beginning of the reduction temperature of ceria, as evidenced from TPR results. This was previously studied, and it was reported that the desorption temperature of $H_2$ on ceria was about 280-311°C [37]. In the case of the $H_2$ production rate, the results also follow the same trend as results as rates of methanol conversion. $H_2$ production rates were similar for the bare ceria supports, because of the limitation in terms of ceria's reducibility and methanol decomposition at specific temperature. It is reported that oxidation reactions on the ceria surface proceed *via* the Mars-van Krevelen mechanism, where an adsorbate reacts with lattice oxygen on the ceria surface, followed by product desorption. Subsequently, oxygen lattice vacancies at the surface are replaced by $O_2$ from the gas phase to close the catalytic cycle [11, 38]. Interestingly, the $H_2$ production

rate substantially improved by about 2-fold for the corresponding series of catalysts containing gold. $Au/CeO_2$-0.135 had the greatest $H_2$ production rate over the temperature range 200-400°C. This result is in agreement with previous work that the highest methanol conversion and hydrogen yield in the OSRM reaction were obtained for an $Au/CeO_2$ catalyst having a gold particle size of about 8 nm [10]. The $H_2$ production rate in the present work is lower than Cu-based catalysts because of different testing conditions in terms of feed composition and space velocity. The 17.3% $Cu/SiO_2$ provided 0.0102 mol $H_2/min{\cdot}g_{cat}$ for OSRM reaction at 250 °C with the molar ratio of $H_2O/MeOH/O_2$: 2/1/0.25 and 60,000 $ml/h{\cdot}g_{cat}$ [39]. Whereas, conventional $Cu\text{-}ZnO/\alpha\text{-}Al_2O_3$ catalysts could produce $H_2$ 0.003 $mol/min{\cdot}g_{cat}$ at 200 °C for the OSRM reaction at space velocity of 31500 $mL/h{\cdot}g_{cat}$[40].

Product distribution of $Au/CeO_2$ catalysts is demonstrated in Fig.9. The $H_2$ selectivity of all catalysts were varied as 51.5-59.1%. The higher $H_2$ selectivity of $Au/CeO_2$-0.135 could be observed at 200-250°C in Fig.9a, which might correlate to the greater reducibility of catalyst. The easier migration of oxygen can effectively activate the oxidation reaction and then induce oxygen vacancies that might initiate WGS/SRM reaction. A small amount of $CH_4$ generated less than 1% as a result of the reactivity of SRM product between $H_2$ and CO. The trend of $CO_2$ selectivity reduced along with reaction temperature. Whereas, the CO selectivity increased indicating more favorable methanol decomposition at higher temperature.

The catalytic activity of $Au/CeO_2$ catalysts in the OSRM reaction was also tested at low temperature (100°C). Interestingly, all $Au/CeO_2$ catalysts produced high MeOH conversion (46.5-56.3%), as given in Table 4. The reaction rate of MeOH consumption of $Au/CeO_2$-0.135 and $Au/CeO_2$-0.270 is higher than $Au/CeO_2$-0.540 and $Au/CeO_2$-1.080 catalysts. It implies that our catalysts are more active at lower reaction temperatures compared to other catalysts. The 5-40%

$Cu/CeO_2 \cdot Al_2O_3$ catalysts were also tested in the OSRM reaction at 100°C. Only 4.4-6.6 % MeOH conversion was obtained and the reaction rate of MeOH consumption was only in the range of 0.017-0.025 mmol/min·$g_{cat}$ [36]. Moreover, the light-off temperature for $CuO/CeO_2$ catalysts in the OSRM reaction started at 160°C [33]. Whereas, the CuZnO introduced by Au and $ZrO_2$ had the light-off temperature >100°C for POM reaction [41].

*3.2.1. Reactivity of Au/$CeO_2$-X catalysts in the OSRM reaction at low reaction temperature*

Typically, oxidation reactions are favored at lower temperature due to their exothermic nature, and the opposite for steam reforming of methanol, because it is an endothermic reaction. Therefore, the capability of the catalyst to exhibit activity for oxidation at lower temperature relies on the oxygen mobility within the cubic fluorite ceria structure. This key feature of oxygen lattice mobility and redox behavior are important for the oxidation activity.

Different levels of methanol conversion were observed at 200°C. These differences may be correlated with the improved redox properties of catalysts, as these are necessary for the oxidation reaction, due to exchange of oxygen within the structure and the role of participating active oxygen in the reaction. It has been proposed that the lattice oxygen of ceria is responsible for stabilizing a hydrogen atom. Whereas, the oxygen vacancies act as an adsorption site for an intermediate methoxy species [1]. Therefore, $Au/CeO_2$-0.135 and 0.270 exhibited higher methanol conversion than other catalysts as summarized in Table 4, because they had the highest $H_2$ uptake when normalized for surface area. These unique properties can promote the OSRM activity.. Moreover, the catalyst surface area normalized $H_2$ uptake also influenced the selectivity of $H_2/CO_2$ formation (Table 4). The highest $H_2/CO_2$ formation was also shown by $Au/CeO_2$-0.135 (1.43), and it decreased in the following order:

$Au/CeO_2$-0.135 (1.43) > $Au/CeO_2$-0.270 (1.38) > $Au/CeO_2$-1.080 (1.23) > $Au/CeO_2$-0.540 (1.11)

However, the ratio of $H_2/CO_2$ was lower than the theoretical value, which is in the range 2-3, for the combination of SRM and POM reactions, indicating the reaction pathway did not mainly proceed *via* POM and subsequently alternative steam reforming of methanol. The reason for the higher $CO_2$ formation in the product stream may be that additional side reactions, such as the WGS, may also operate. The sources of CO formation at low temperature can come from either methanol decomposition reaction or incomplete combustion. CO formation and increasing $H_2O$ ratio due to by-product of combustion can sufficiently drive the thermodynamic equilibrium for the WGS reaction. It could promote the low temperature WGS reaction, which normally was in the range of 180-250°C for Au and Cu catalysts [42, 43]. Therefore, the WGS reaction may play a key role in determining $H_2/CO_2$ selectivity at the lowest temperature, due to its slightly exothermic nature. One of the most important energy barriers for this reaction is dissociation of water into OH and H on the ceria surface [44]. Consequently, the low temperature WGS proceeds *via* CO reacting with OH to form OHCO as an intermediate species and then desorbs as $CO_2$ gas. Whereas, 2 H atoms combine together and then desorb as $H_2$ gas. It was postulated that the metal surface can effectively bind CO near the interface and react with OH located at the oxygen vacancies adjacent to the metal atom [45]. This can support the reactivity of the WGS reaction.

The selective $H_2$ formation might be significantly influenced by the WGS reaction. This aspect of $Au/CeO_2$ catalysts for WGS were emphasized, such as the interface between $Au/CeO_2$, available active surface of ceria and the oxidation state of Au. The cationic gold species might be responsible for higher activity of $H_2$ production at the lowest reaction temperature as seen in Fig.9a. The cationic gold species were previously reported as the active state for WGS reaction [46]. However, they were an unstable and could be easily reduced to the metallic phase under WGS reaction [47].

Hence, the $H_2$ selectivity of Au/$CeO_2$-0.135 has a high value at low temperature, and then dropped at higher reaction temperature. Whereas, the $H_2$ selectivity of Au/$CeO_2$-0.540 was lower at the lowest temperature in comparison with others, and then it increased at higher temperature. This is probably relevant to the dominant $Au^0$ species, which was considered as more stable gold state, resulting in a relatively stable catalyst at high temperature. The deactivation of Au catalysts in the WGS reactionat lower temperature was due to less available surface area of ceria, and strong adsorption of $CO_2$ could block the active sites for dissociative water adsorption leading to a slower rate [48]. While the loss of WGS activity at high temperature was affected by the destruction of Au/$CeO_2$ interactions due to the lost contact at the interface between Au and ceria (most probably cationic gold).

*3.2.2. The role of Au in the OSRM reaction*

In the present study, the surface analysis by XPS showed the distribution of Au species, which include $Au^0$, $Au^+$, and $Au^{3+}$ for the Au/$CeO_2$ catalysts. It is observed that the catalyst having the highest $Au^{n+}/Au^0$ ratio had a very high catalytic activity compared to the other catalysts. This agrees well with our previous work for preferential CO oxidation [7], OSRM [10] and SRM [2] studies catalyzed by Au on different $CeO_2$ morphologies. Several studies have proposed that the active site for catalytic reactions occurred on the perimeter of the gold particle with the oxide interface [48-50]. As the cationic gold is less stable than metallic gold, there are literature reports that the formation of $H_2$ on cationic gold caused the reduction of cationic gold to metallic gold for Au/$CeO_x$-$TiO_2$ and Au/Ce(Gd)$O_x$ for the WGS reaction [47, 51]. The oxidic gold is related to the interaction between a gold ion and an oxygen atom. The oxidation state of Au can also be influenced by gold particle size and how well-dispersed particles are on the supports.

Corresponding to the TEM images, the smaller gold particles are present on the active surface (200) for Au/$CeO_2$-0.135. Whilst, significantly larger sized gold particles (13.2 nm) were present on the most stable (111) surface for Au/$CeO_2$-1.080. This indicates that the more active (200) ceria surface can disperse gold particles to a greater extent than the less active (111) ceria surface. Moreover, this increased dispersion resulted in improving redox properties for ceria after gold incorporation. Au supported on ceria prepared with lower CTAB concentration had greater redox-properties, as evidenced from the higher amount of $H_2$-uptake in Table 2. The improvement of redox properties related to the dispersion of Au particles on a ceria support has been reported previously [6]. Moreover, it represents the presence of loosely oxygen bound species on the ceria surface and oxygen mobility within the structure.

However, the optimum gold size for the specific reaction is still debated. The current study found that the highest methanol conversion and hydrogen yield were obtained with small gold particle sizes of 7.9 nm, in the same way reported previously for 3%Au/$CeO_2$ in the OSRM reaction [10]. The gold particle size has an important influence on activity, for example, supported gold catalysts, with small gold nanoparticles of less than 5 nm, showed high catalytic activity for partial oxidation of methanol to produce hydrogen [15, 52]. Oxygen adsorbed on oxide supports was also more readily available in the case of small Au particles [2]. Haruta *et al.* proposed that CO oxidation proceeded at the interface between the gold nanoparticle and the ceria support, with smaller sized gold nanoparticles less than 5 nm being the most active [49]. The small gold particle size might play a key role for providing active sites for the SRM reaction. The interaction between smaller gold particles and ceria support is beneficial compared to larger gold particles, resulting in weakening of the Ce-O bond to generate oxygen vacancies adjacent to the gold particle. Surface gold and oxygen vacancies participate in promoting the catalytic activity by stabilizing an

intermediate species. Furthermore, the more loosely bound oxygen species on the surface can facilitate the conversion of intermediate species in the SRM reaction [1].

## 4. Conclusion

Hydrothermal CTAB surfactant assisted synthesis of Bundle-like ceria nanorods can reduce particle agglomeration, leading to better physical properties and higher surface area. However, higher concentrations of CTAB (>0.270 mmol) can form ceria with less favorable properties, due to suppression of ion diffusion during synthesis crystallization. The properties of $CeO_2$-0.135 resulted in formation of a catalyst that most effectively dispersed gold to give the best performance for OSRM. The more active (200) surface of the ceria nanorods can disperse gold to a greater extent, producing smaller gold particles exposing the (111) and (200) crystal planes, and a higher concentration of cationic gold species. The active site of cationic gold, smaller gold particle size and improved redox properties played a major role in determining better catalytic activity, characterized by higher methanol conversion and $H_2$ content for OSRM at the lowest temperature of 200˚C.

## Acknowledgements

The work was supported by the Ratchadaphiseksomphot Endowment Fund, Chulalongkorn University (CU-GES-60-04-63-03). The authors thank the Thailand Research Fund (TRF) and National Science and Technology Development Agency (PHD/0237/2558) for the scholarship funding of Ms. Srisin Eaimsumang. We are grateful to Dr. Thomas David, the School of Chemistry, Cardiff University, UK for technical support of HR-TEM.

**References**


[1] N. Yi, R. Si, H. Saltsburg, M. Flytzani-Stephanopoulos, Appl. Catal. B Environ., 95 (2010) 87.

[2] N. Yi, R. Si, H. Saltsburg, M. Flytzani-Stephanopoulos, Energy Environ. Sci., 3 (2010) 831.

[3] D. Andreeva, V. Idakiev, T. Tabakova, L. Ilieva, P. Falaras, A. Bourlinos, A. Travlos, Catal. Today, 72 (2002) 51.

[4] A. Luengnaruemitchai, S. Osuwan, E. Gulari, Catal. Commun., 4 (2003) 215.

[5] H.Y. Kim, G. Henkelman, J Phys Chem Lett., 3 (2012) 2194.

[6] F. Yinga, S. Wang, C.-T. Au, S.-Y. Lai, Gold Bull., 43 (2010) 241.

[7] M. Carltonbird, S. Eaimsumang, S. Pongstabodee, S. Boonyuen, S.M. Smith, A. Luengnaruemitchai, Chem. Eng. J., 344 (2018) 545.

[8] A. Luengnaruemitchai, S. Osuwan, E. Gulari, Int. J. Hydrog. Energy, 29 (2004) 429.

[9] C. Pojanavaraphan, A. Luengnaruemitchai, E. Gulari, Chem. Eng. J., 192 (2012) 105.

[10] S. Eaimsumang, S. Wongkasemjit, S. Pongstabodee, S. MeejooSmith, S. Ratanawilai, N. Chollacoop, A. Luengnaruemitchai, J. Rare Earths, 37 (2019) 819.

[11] D.R. Mullins, Surf. Sci. Rep., 70 (2015) 42.

[12] S. Agarwal, B.L. Mojet, L. Lefferts, A.K. Datye, Chapter 2 - Ceria nanoshapes—structural and catalytic properties, in: Z. Wu, S.H. Overbury (Eds.) Catalysis by Materials with Well-Defined Structures, Elsevier, Amsterdam, 2015, pp. 31.

[13] Z. Guo, F. Du, Z. Cui, Mater. Lett., 61 (2007) 694.

[14] A.A. Tillirou, C.R. Theocharis, Adsorp Sci Technol, 26 (2008) 687.

[15] T.C. Ou, F.W. Chang, L.S. Roselin, J. Mol. Catal. A: Chem., 293 (2008) 8.

[16] G. Leofanti, M. Padovan, G. Tozzola, B. Venturelli, Catal. Today, 41 (1998) 207.

[17] C.S. Pan, D.S. Zhang, L.Y. Shi, J. Solid State Chem., 181 (2008) 1298.

[18] S.R. Ede, U. Nithiyanantham, S. Kundu, PCCP, 16 (2014) 22723.

[19] M. Lin, Z.Y. Fu, H.R. Tan, J.P.Y. Tan, S.C. Ng, E. Teo, Cryst. Growth Des., 12 (2012) 3296.

[20] N. Garti, H. Zour, J. Cryst. Growth, 172 (1997) 486.

[21] W.-J. Li, E.-W. Shi, T. Fukuda, Cryst. Res. Technol., 38 (2003) 847.

[22] M.Y. Cui, J.X. He, N.P. Lu, Y.Y. Zheng, W.J. Dong, W.H. Tang, B.Y. Chen, C.R. Li, Mater. Chem. Phys., 121 (2010) 314.

[23] S. Scirè, S. Minicò, C. Crisafulli, C. Satriano, A. Pistone, Appl. Catal. B Environ., 40 (2003) 43.

[24] C.T. Nottbohm, C. Hess, Catal. Commun., 22 (2012) 39.

[25] S. Chen, L. Li, W. Hu, X. Huang, Q. Li, Y. Xu, Y. Zuo, G. Li, ACS Appl. Mater. Interfaces, 7 (2015) 22999.

[26] R.B. Zhang, K. Lu, L.J. Zong, S. Tong, X.W. Wang, J. Zhou, Z.H. Lu, G. Feng, J. Mol. Catal., 442 (2017) 173.

[27] C. Schilling, A. Hofmann, C. Hess, M.V. Ganduglia-Pirovano, J. Phys. Chem. C, 121 (2017) 20834.

[28] Q. Fu, H. Saltsburg, M. Flytzani-Stephanopoulos, Science, 301 (2003) 935.

[29] X.S. Huang, H. Sun, L.C. Wang, Y.M. Liu, K.N. Fan, Y. Cao, Appl. Catal. B Environ., 90 (2009) 224.

[30] A. Longo, L.F. Liotta, G. Pantaleo, F. Giannici, A.M. Venezia, A. Martorana, J. Phys. Chem. C, 116 (2012) 2960.

[31] W. Zhang, X. Niu, L. Chen, F. Yuan, Y. Zhu, Sci. Rep., 6 (2016) 29062.

[32] R. Pérez-Hernández, A. Gutiérrez-Martínez, C.E. Gutiérrez-Wing, Int. J. Hydrog. Energy, 32 (2007) 2888.

[33] P.P.C. Udani, P.V.D.S. Gunawardana, H.C. Lee, D.H. Kim, Int. J. Hydrog. Energy, 34 (2009) 7648.

[34] R. Pérez-Hernández, A. Gutiérrez-Martínez, M.E. Espinosa-Pesqueira, M.L. Estanislao, J. Palacios, Catal. Today, 250 (2015) 166.

[35] C. Cammarano, G. Bagnasco, M. Turco, E. Moretti, L. Storaro, A. Talon, M. Lenarda, One-step synthesized CuO-$CeO_2$-$Al2O_3$ system as catalyst for OSRM process, in, 2008.

[36] P. Mierczynski, M. Mosinska, W. Maniukiewicz, M. Nowosielska, A. Czylkowska, M.I. Szynkowska, React Kinet Mech Cat., 127 (2019) 857.

[37] D.G. Araiza, A. Gómez-Cortés, G. Díaz, Catal. Today, 282 (2017) 185.

[38] C. Doornkamp, V. Ponec, J. Mol. Catal. A: Chem., 162 (2000) 19.

[39] L. Selva Roselin, H.-W. Chiu, J. Saudi Chem. Soc., 22 (2017) 692.

[40] J.B. Wang, C.-H. Li, T.-J. Huang, Catal. Lett., 103 (2005) 239.

[41] H.-Y. Huang, H.-I. Chen, Y.-J. Huang, Catalysts, 8 (2018).

[42] A.M. Abdel-Mageed, G. Kučerová, J. Bansmann, R.J. Behm, ACS Catal., 7 (2017) 6471.

[43] A. Jha, D.-W. Jeong, J.-O. Shim, W.-J. Jang, Y.-L. Lee, C.V. Rode, H.-S. Roh, Catal. Sci. Technol., 5 (2015) 2752.

[44] J.A. Rodriguez, P. Liu, J. Hrbek, J. Evans, M. Pérez, Angew. Chem. Int. Ed., 46 (2007) 1329.

[45] K.G. Azzam, I.V. Babich, K. Seshan, L. Lefferts, J. Catal., 251 (2007) 153.

[46] Q. Fu, W. Deng, H. Saltsburg, M. Flytzani-Stephanopoulos, Appl. Catal. B Environ., 56 (2005) 57.

[47] R. Si, J. Tao, J. Evans, J.B. Park, L. Barrio, J.C. Hanson, Y.M. Zhu, J. Hrbek, J.A. Rodriguez, J. Phys. Chem. C, 116 (2012) 23547.

[48] R. Burch, PCCP, 8 (2006) 5483.

[49] M. Haruta, Catal. Today, 36 (1997) 153.

[50] L.M. Molina, B. Hammer, Appl. Catal., A., 291 (2005) 21.

[51] Q. Wang, J.C. Hanson, A.I. Frenkel, J. Chem. Phys., 129 (2008) 234502.

[52] E. Hernández-Ramírez, J.A. Wang, L.F. Chen, M.A. Valenzuela, A.K. Dalai, Appl. Surf. Sci., 399 (2017) 77.

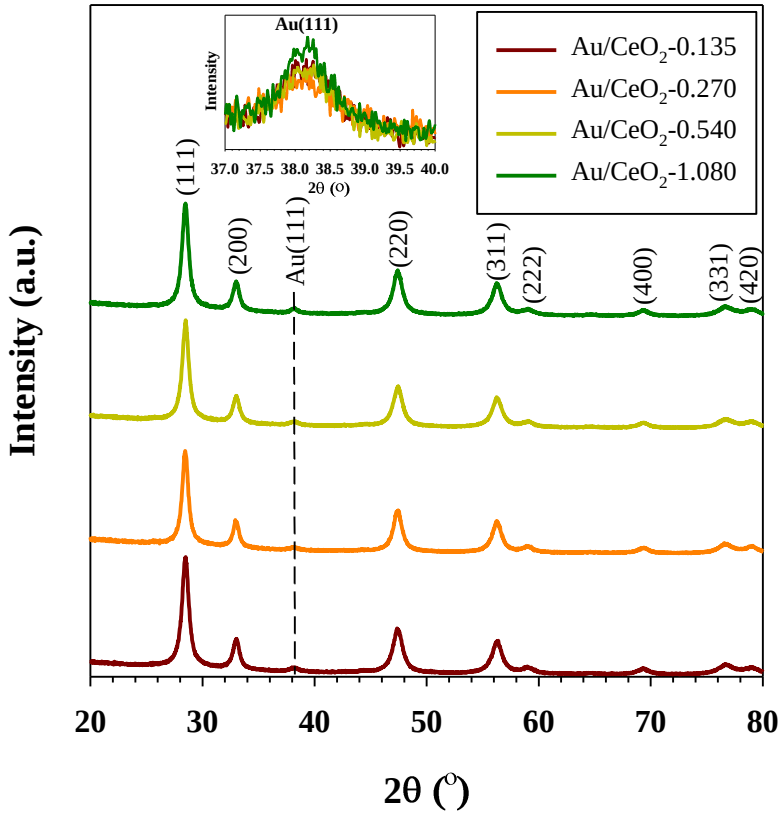


**Fig.1** Representative powder XRD patterns of the $Au/CeO_2$ catalysts

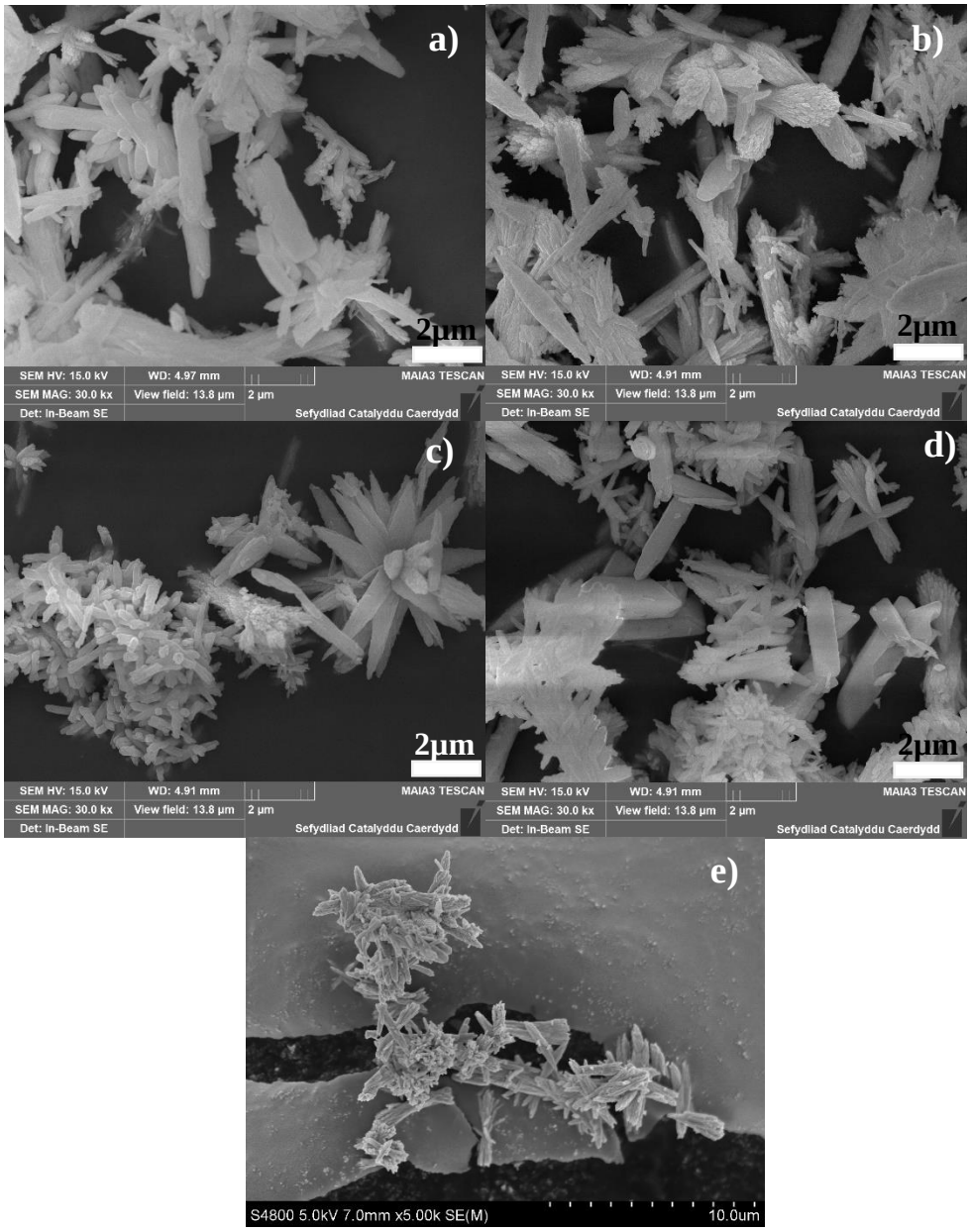


**Fig. 2** Representative SEM images of ceria synthesized at various CTAB concentrations at magnification of 30k of a) $CeO_2$-0.135, b) $CeO_2$-0.270, c) $CeO_2$-0.540, d) $CeO_2$-1.08 and at 5.0k of e) $CeO_2$-0.000

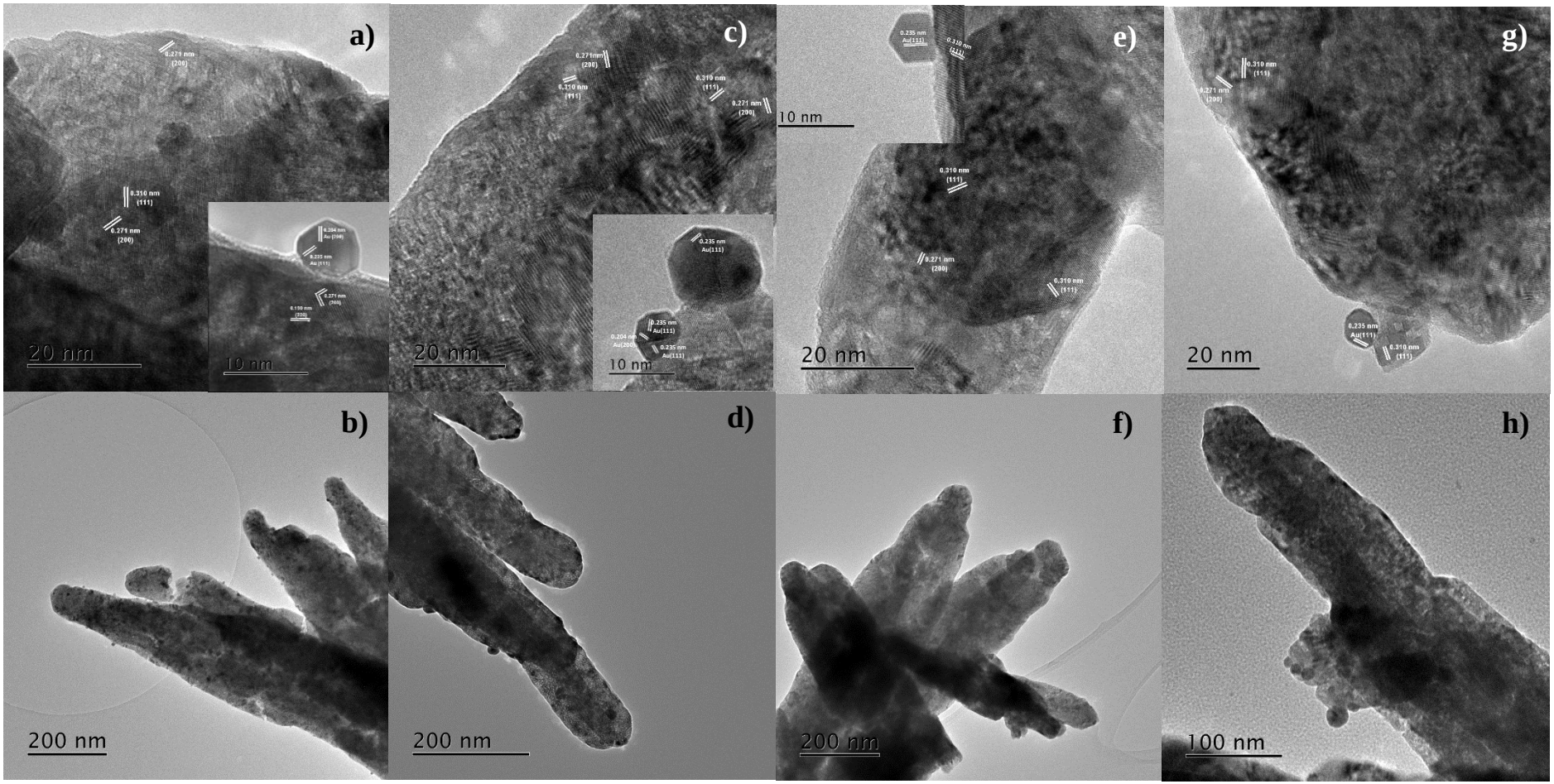


**Fig. 3** Representative HR-TEM images to identify crystal-planes and morphologies of (a,b) Au/$CeO_2$ -0.135, (c,d) Au/$CeO_2$-0.270, (e,f) Au/$CeO_2$-0.540 and (g,h) Au/$CeO_2$-1.080 catalysts

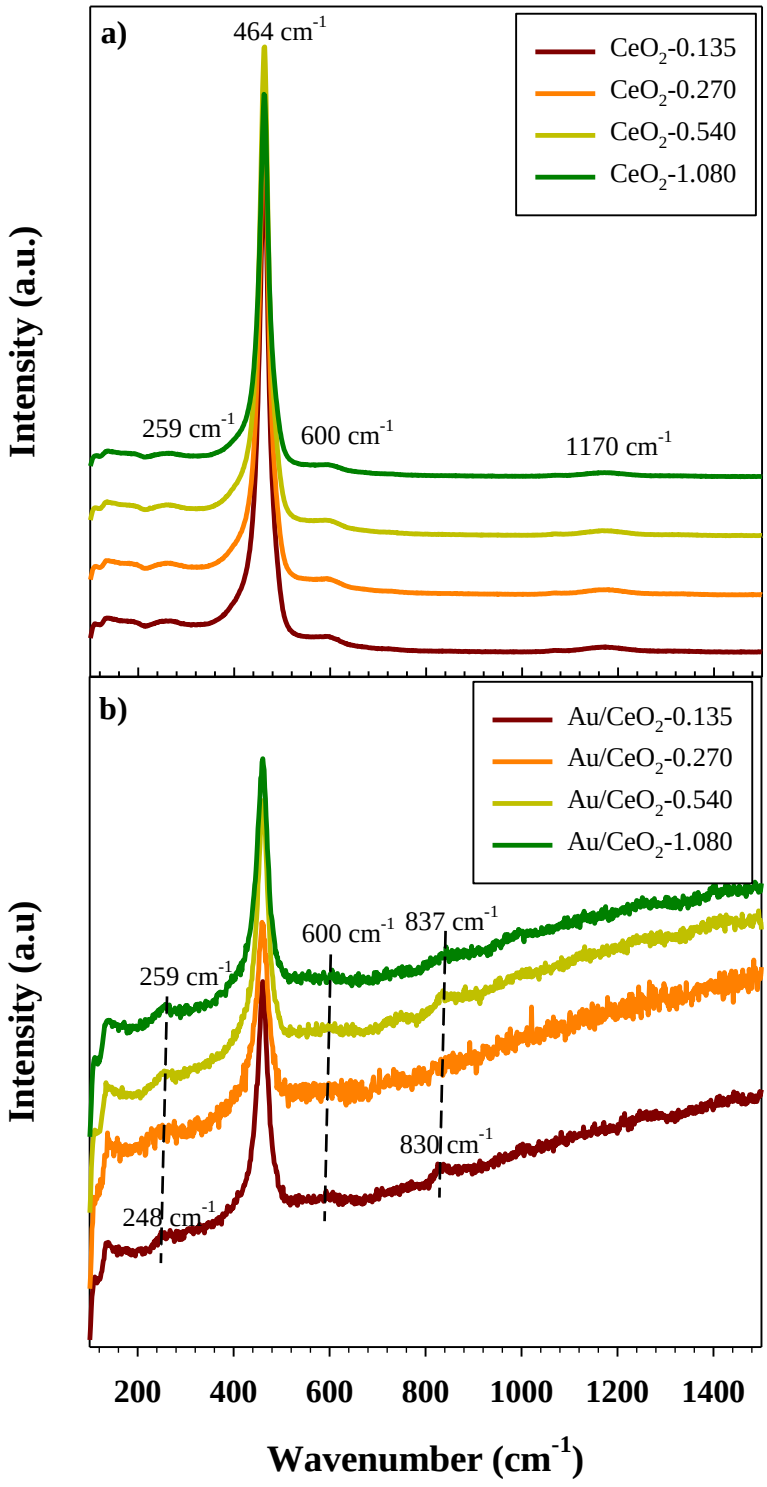


**Fig. 4** Representative Raman spectra of the $CeO_2$-X supports and Au/$CeO_2$-X catalysts

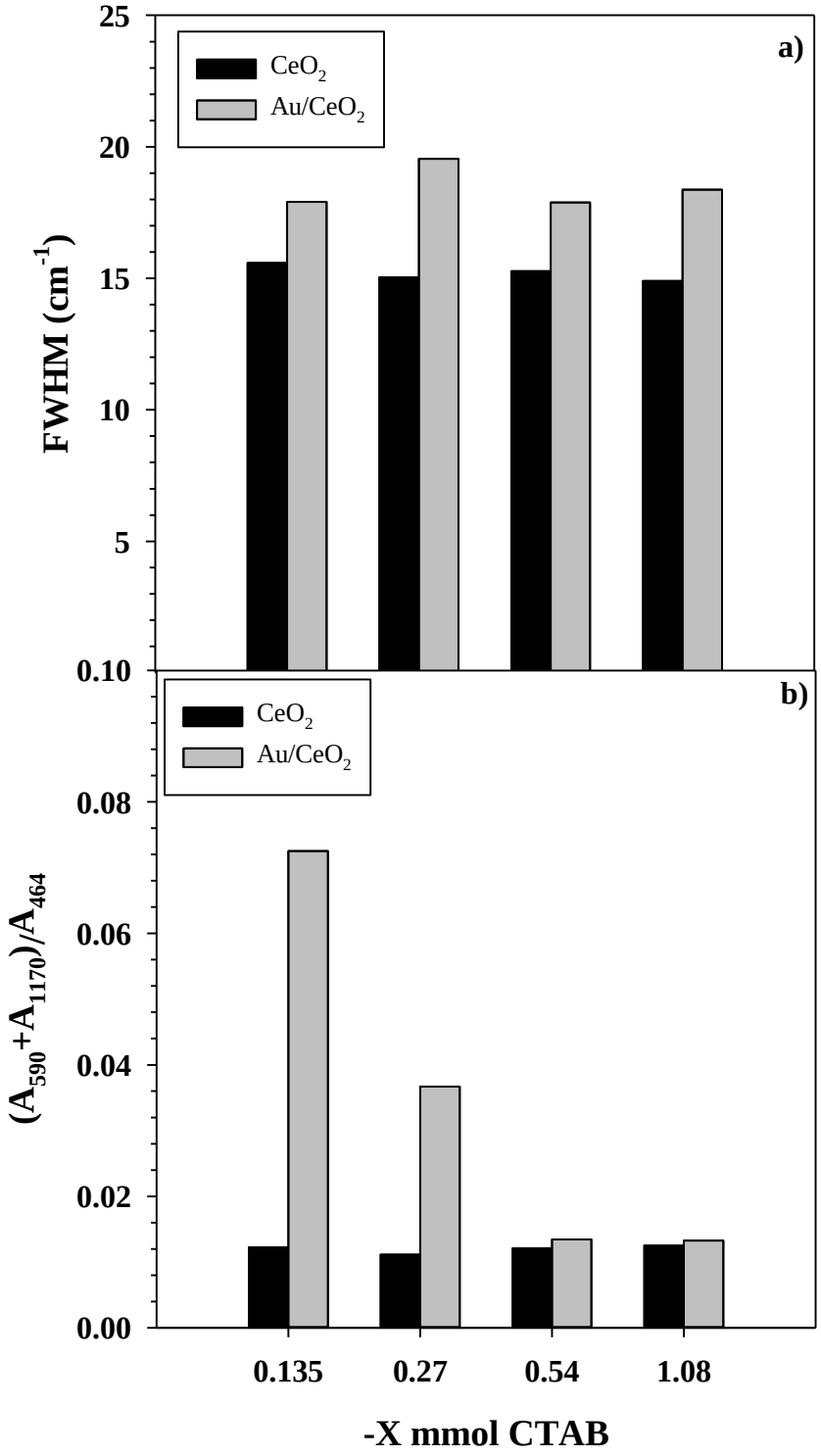


**Fig.5** Representative comparison of (a) FWHM and (b) defect concentration between the $CeO_2$-X and Au/$CeO_2$-X catalysts, determined from Raman spectra

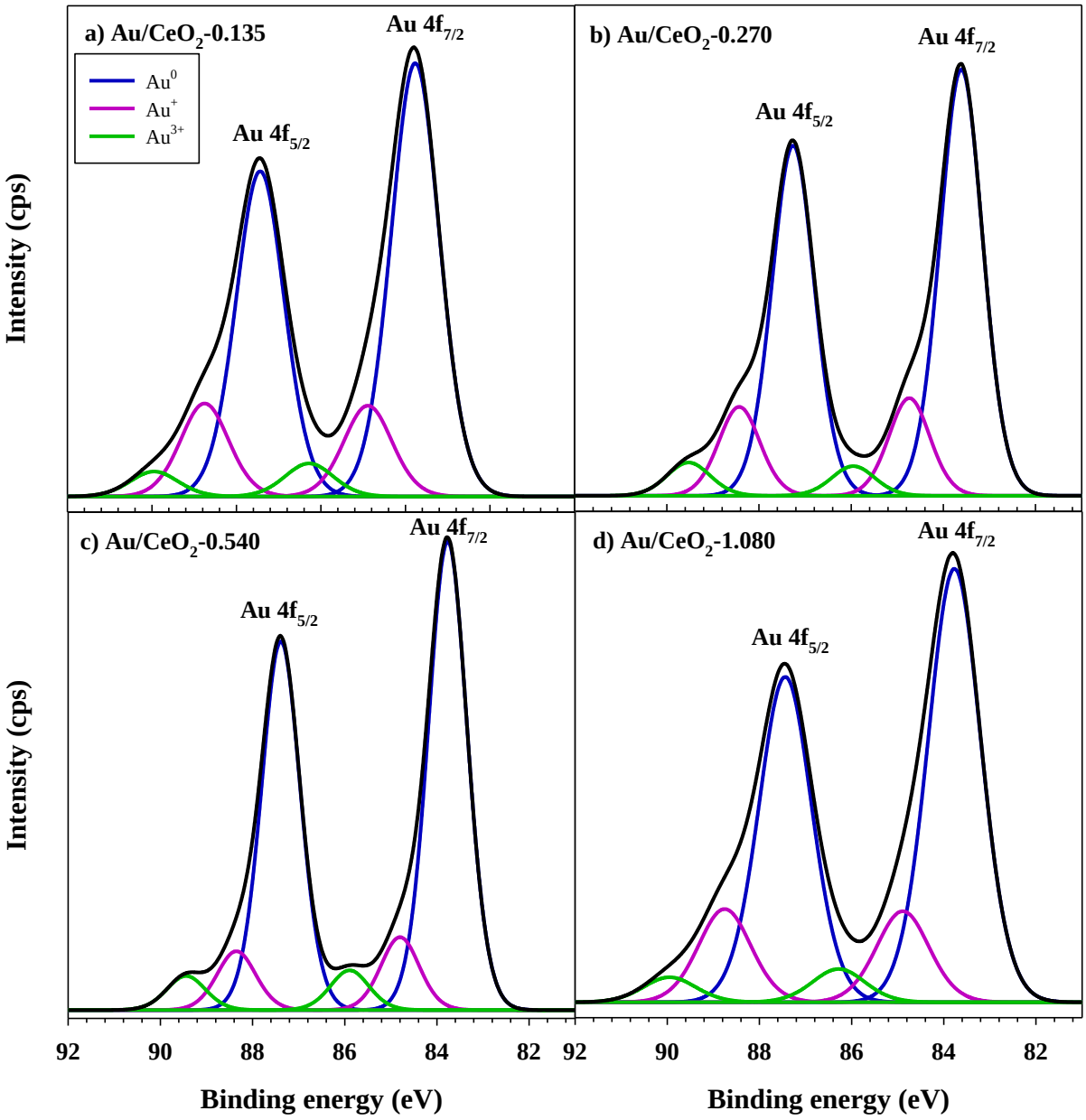


**Fig. 6** Representative Au4f XP spectra of the Au/$CeO_2$-X catalysts

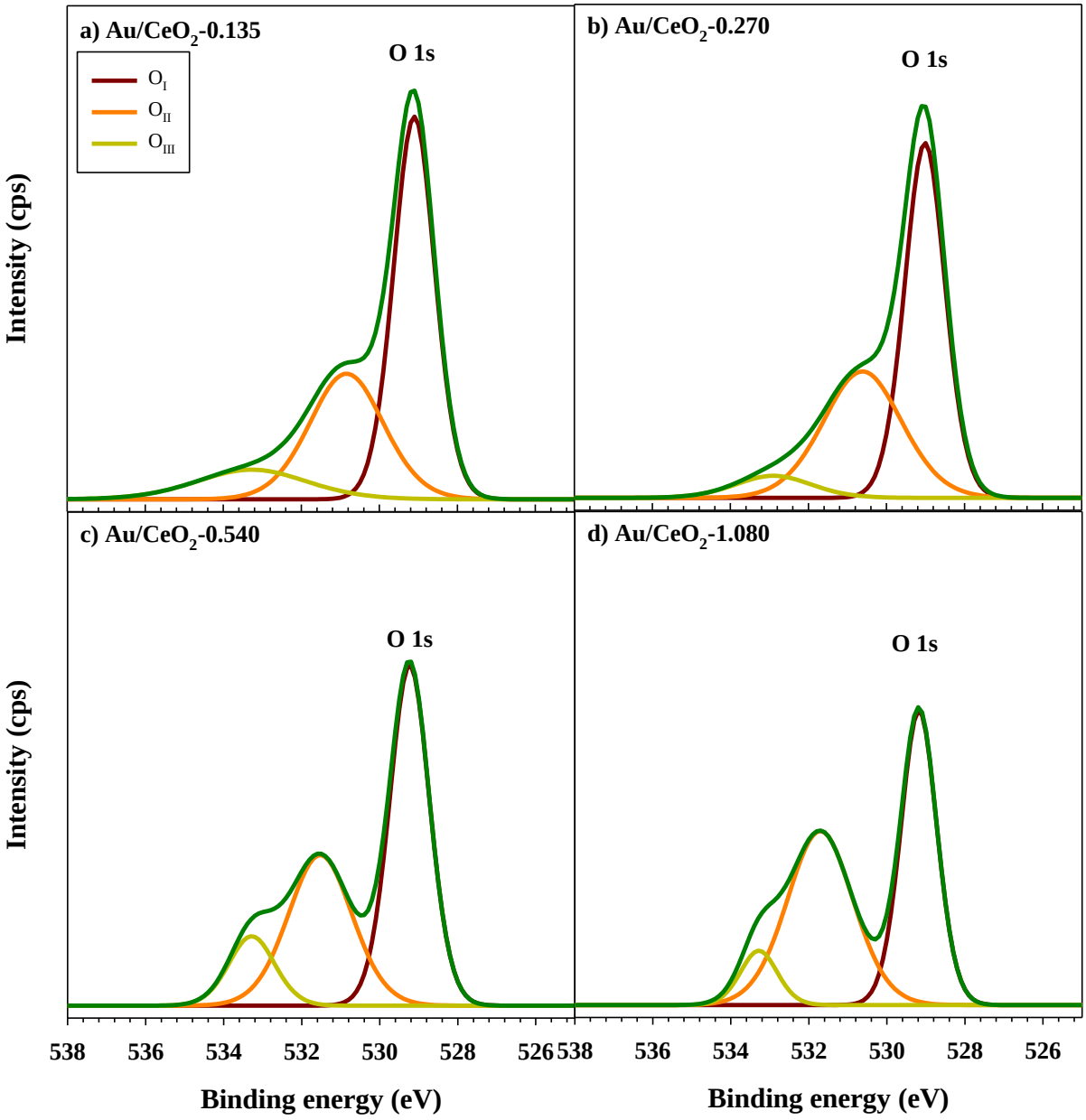


**Fig. 7** Representative O 1s XP spectra of the Au/$CeO_2$-X catalysts

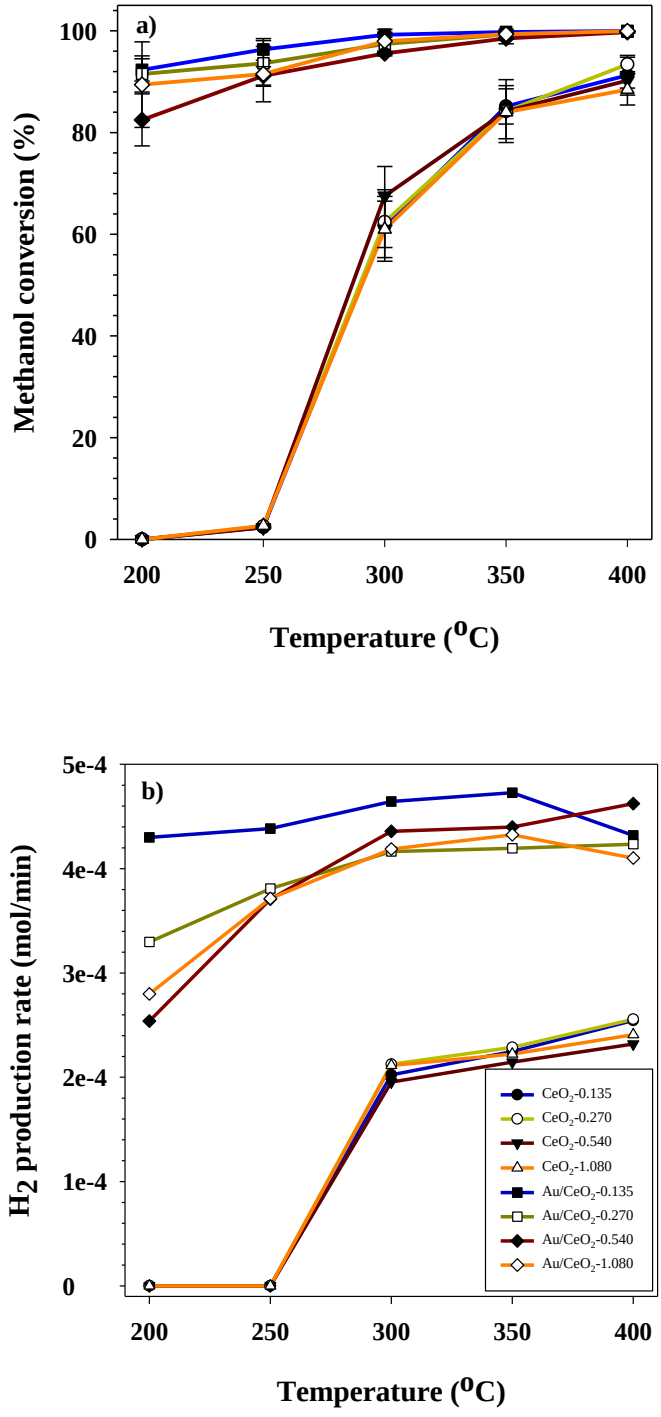


**Fig. 8** Catalytic activity of the $CeO_2$-X supports and Au/$CeO_2$-X catalysts for the OSRM reaction at GSHV = 30,000 mL/g.h as measured in terms of a) methanol conversion (%) and b) $H_2$ production rate (mol/min)

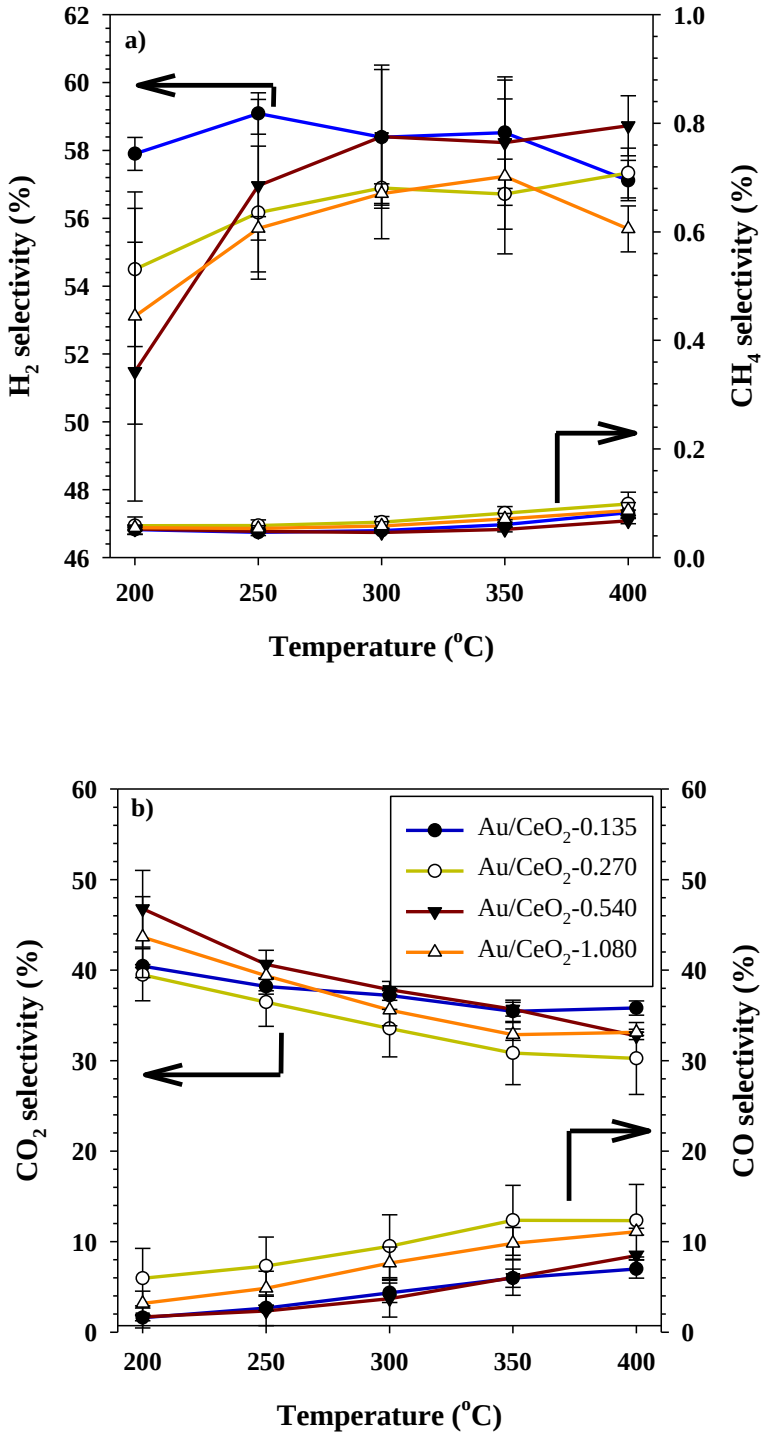


**Fig. 9** Product selectivities of the $CeO_2$-X and Au/$CeO_2$-X catalysts for OSRM reaction between 200-400ºC.

**Table 1 Physicochemical properties of the $CeO_2$-X supports and Au/$CeO_2$-X catalysts**

| Sample- CTAB (mmol) | [a]$D_{(111)}$ (nm) | [b]$D_{Au(111)\ (nm)}$ | [c]$D_{Au}$ | $S_{BET}$ ($m^2/g$) | [d]Au loding (wt%) |
|---|---|---|---|---|---|
| $CeO_2$ w/o CTAB | 12.3 | N/A | N/A | 56 | N/A |
| $CeO_2$-0.135 | 11.6 | N/A | N/A | 89 | N/A |
| $CeO_2$-0.270 | 12.4 | N/A | N/A | 90 | N/A |
| $CeO_2$-0.540 | 12.0 | N/A | N/A | 75 | N/A |
| $CeO_2$-1.080 | 11.8 | N/A | N/A | 78 | N/A |
| Au/$CeO_2$-0.135 | 12.1 | 8.8 | 7.9 | 81 | 2.38 |
| Au/$CeO_2$-0.270 | 13.4 | 8.3 | 7.8 | 76 | 2.45 |
| Au/$CeO_2$-0.540 | 12.0 | 9.4 | 8.7 | 82 | 2.35 |
| Au/$CeO_2$-1.080 | 12.1 | 11.9 | 13.1 | 66 | 2.29 |

[a] crystallite size of ceria determined by Sherrer's equation from (111) diffraction peak of ceria

[b] Au crystallite size calculated by Sherrer's equation from Au (111)

[c] average gold crystallite size measured by counting 50 particles on HR-TEM images by means of particle size distribution

[d] actual gold loading determined by ICP-EOS

**Table 2 Summary of catalyst reducibility from Temperature Programmed Reduction studies**

| Sample- CTAB (mM) | Peak maximum (˚C)[a] | $H_2$ uptake (mmol/g) | $H_2$ uptake/$S_{BET}$ (mmol/$m^2$) |
|---|---|---|---|
| $CeO_2$-0.135 | 519 | 0.48 | 0.0054 |
| $CeO_2$-0.270 | 519 | 0.50 | 0.0056 |
| $CeO_2$-0.540 | 520 | 0.49 | 0.0065 |
| $CeO_2$-1.080 | 519 | 0.42 | 0.0053 |
| Au/$CeO_2$-0.135 | 148 | 0.82 | 0.0101 |
| Au/$CeO_2$-0.270 | 146 | 0.62 | 0.0082 |
| Au/$CeO_2$-0.540 | 145 | 0.28 | 0.0035 |
| Au/$CeO_2$-1.080 | 154 | 0.53 | 0.0080 |

[a] peak maximum for ceria surface reduction

**Table 3 Summary of elemental surface composition from X-ray Photoelectron Spectroscopy analysis**

| Sample | Au (at %) | Ce (at%) | O (at%) | $Au^0$ (at%) | $Au^+$ (at%) | $Au^{3+}$ (at%) | $Au^{n+}/Au^0$ | $Ce^{3+}$ (%) | $O_I$(%) |
|---|---|---|---|---|---|---|---|---|---|
| Au/$CeO_2$-0.135 | 1.32 | 26.55 | 72.13 | 70 | 25.9 | 4.1 | 0.43 | 23.5 | 55.7 |
| Au/$CeO_2$-0.270 | 0.81 | 24.82 | 74.37 | 76 | 17.8 | 6.3 | 0.32 | 18.0 | 55.2 |
| Au/$CeO_2$-0.540 | 1.12 | 23.19 | 75.69 | 81.6 | 3.8 | 14.6 | 0.23 | 13.9 | 51.5 |
| Au/$CeO_2$-1.080 | 0.84 | 20.36 | 78.80 | 76.3 | 18.4 | 5.8 | 0.31 | 22.1 | 44.2 |

**Table 4 the catalytic activity of $Au/CeO_2$ catalysts in OSRM reaction at 100 and 200 °C**

| Sample | MeOH conversion (%) at 100°C | $r_{MeOH}$ (mmol/min·$g_{cat}$) at 100°C | $r_{H2}$ (mmol/min·$g_{cat}$) at 100°C | MeOH conversion at 200°C | $H_2/CO_2$ at 200°C |
|---|---|---|---|---|---|
| $Au/CeO_2$-0.135 | 56.3 | 1.84 | 1.32 | 92.3 | 1.43 |
| $Au/CeO_2$-0.270 | 54.4 | 1.78 | 1.37 | 91.5 | 1.39 |
| $Au/CeO_2$-0.540 | 46.5 | 1.51 | 0.98 | 82.5 | 1.11 |
| $Au/CeO_2$-1.080 | 48.4 | 1.59 | 1.26 | 89.4 | 1.23 |

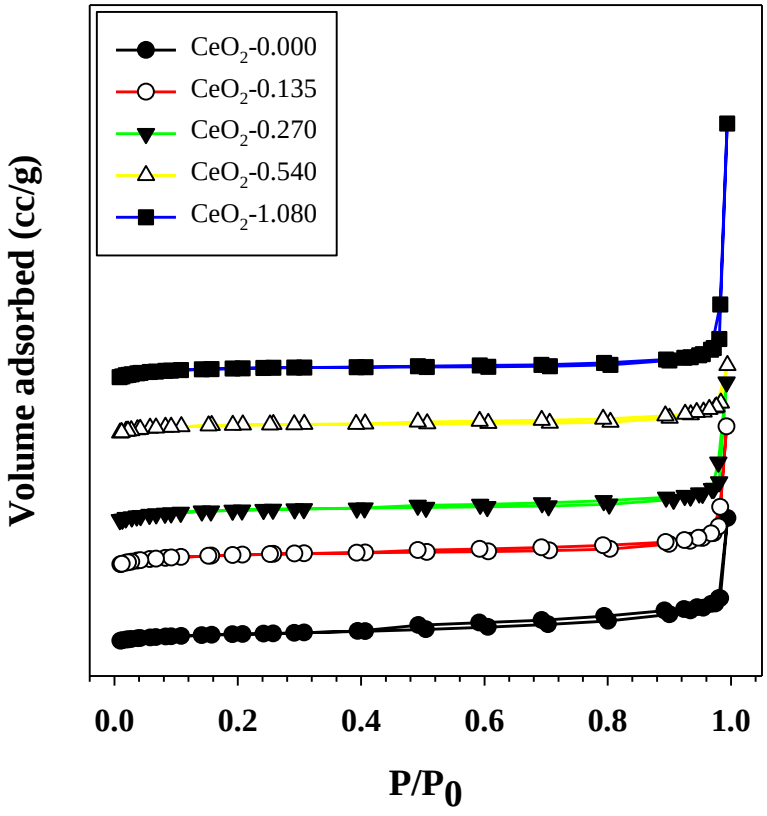


**Fig. SI1** Representative $N_2$- adsorption-desorption isotherms of synthesized $CeO_2$ catalysts

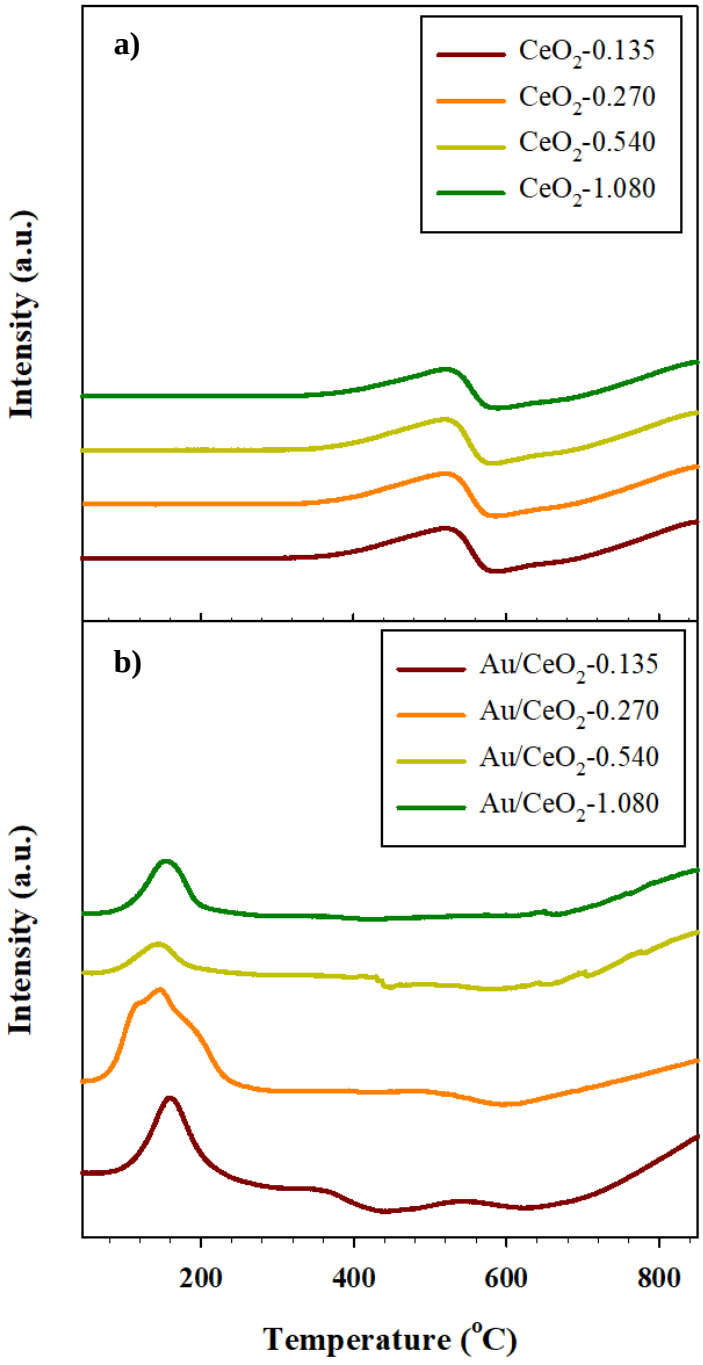


**Fig. SI2** Representative $H_2$-TPR of the (a) $CeO_2$-X supports and (b) Au/$CeO_2$-X catalysts

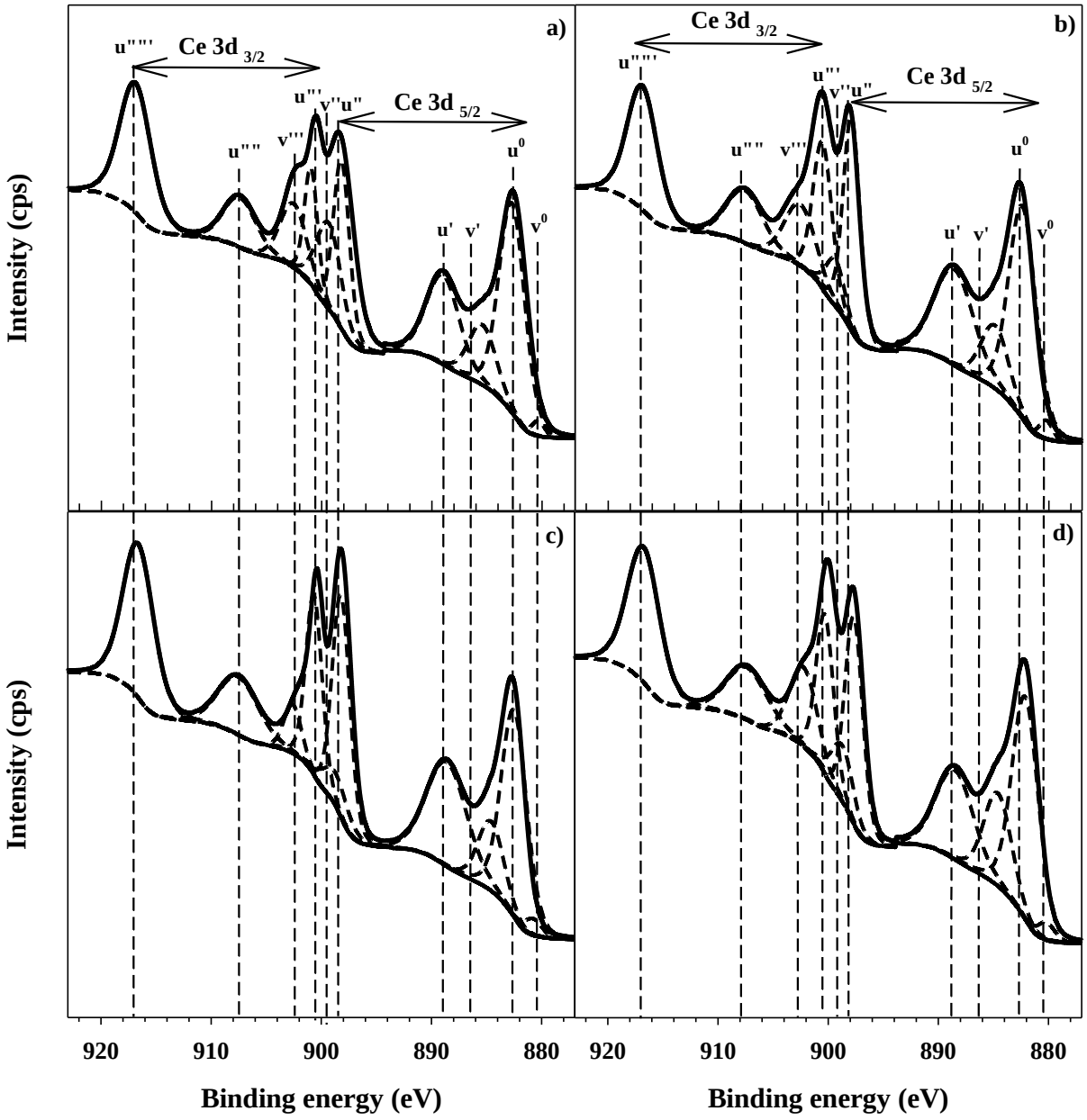


**Fig. SI3** Representative XP spectra of Ce3d of a) Au/$CeO_2$-0.135, b) Au/$CeO_2$-0.270, c) Au/$CeO_2$-0.540 and d) Au/$CeO_2$-1.080 catalysts